JUSTC

Article

http://justc.ustc.edu.cn

Received: November 15, 2021; Accepted: January 21, 2022

Characteristics of clouds, precipitation, and latent heat in midlatitude frontal system mixed with dust storm from GPM satellite observations and WRF simulations

Renjun Zhou[1], Tianyuan Yan[1], Shuping Yang[1], Yunfei Fu[1], Chen Huang[1], Hongxia Zhu[1], and Rui Li[1,2,3] ✉

[1]*School of Earth and Space Sciences, University of Science and Technology of China, Hefei 230026, China;*
[2]*Comparative Planetary Excellence Innovation Center, Chinese Academy of Sciences, Hefei 230026, China;*
[3]*State Key Laboratory of Fire Science, University of Science and Technology of China, Hefei 230026, China*

✉*Correspondence: Rui Li, E-mail: rli7@ustc.edu.cn*

Graphical abstract

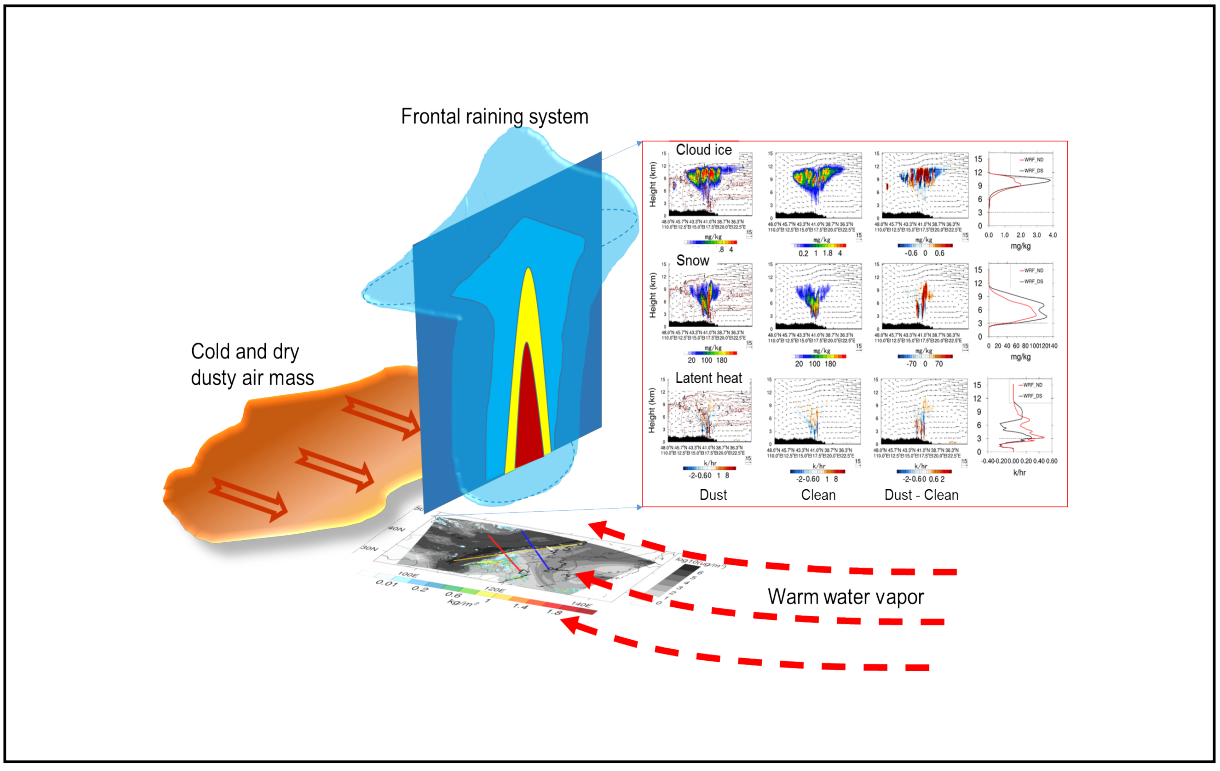

Dust can affect the vertical structure of precipitation and latent heat in frontal raining system.

Public summary

- WRF simulations and GPM observations were combined to study the interactions between dust aerosols and frontal raining system.
- Greater cloud ice, snowfall, high-altitude precipitation rate, and more latent heat rate at upper layers were found in selected dust laden area.
- WRF simulated LH and DPR retrieved LH are comparable in terms of both vertical shape and amplitude in selected vertical cross sections.

Citation: Zhou R J, Yan T Y, Yang S P, et al. Characteristics of clouds, precipitation, and latent heat in midlatitude frontal system mixed with dust storm from GPM satellite observations and WRF simulations. *JUSTC*, **2022**, 52(2): 3. DOI: 10.52396/JUSTC-2021-0238

JUSTC

Article

http://justc.ustc.edu.cn

Received: November 15, 2021; Accepted: January 21, 2022

Characteristics of clouds, precipitation, and latent heat in midlatitude frontal system mixed with dust storm from GPM satellite observations and WRF simulations

Renjun Zhou[1], Tianyuan Yan[1], Shuping Yang[1], Yunfei Fu[1], Chen Huang[1], Hongxia Zhu[1], and Rui Li[1,2,3] ✉

[1]*School of Earth and Space Sciences, University of Science and Technology of China, Hefei 230026, China;*
[2]*Comparative Planetary Excellence Innovation Center, Chinese Academy of Sciences, Hefei 230026, China;*
[3]*State Key Laboratory of Fire Science, University of Science and Technology of China, Hefei 230026, China*

✉*Correspondence: Rui Li, E-mail: rli7@ustc.edu.cn*

Cite This: *JUSTC*, **2022**, 52(2): 3 (14pp) Read Online SI Supporting Information

Abstract: A heavy dust storm originating in Mongolia and Inner Mongolia traveled to Northeast China and met a midlatitude frontal system on May 3, 2017. The potential ice nuclei (IN) effects of mineral dust aerosols on the vertical structure of clouds, precipitation, and latent heat (LH) were studied using Global Precipitation Mission (GPM) satellite observations and Weather Research and Forecasting (WRF) model simulations. The WRF simulations correctly captured the main features of the system, and the surface rain rate distribution was positively correlated with data retrieved from the GPM Microwave Imager. Moreover, the correlation coefficient increased from 0.31 to 0.54 with increasing moving average window size. The WRF-simulated rainfall vertical profiles are generally comparable to the GPM Dual-Frequency Precipitation Radar (DPR) observations, particularly in low layers. The joint probability distribution functions of the rain rate at different altitudes from the WRF simulation and GPM observations show high positive correlation coefficients of ~0.80, indicating that the assumptions regarding the raindrop size distribution in the WRF model and DPR retrieval were consistent. Atmospheric circulation analysis and aerosol optical depth observations from the Himawari-8 satellite indicated that the dust storm entered only a narrow strip of the northwest edge of the frontal precipitation system. The WRF simulations showed that in carefully selected areas of heavy dust, dust can enhance the heterogeneous ice nucleation process and increase the cloud ice, snowfall, high-altitude precipitation rate, and LH rate in the upper layers. This effect is significant at temperatures of −15 °C to −38 °C and requires dust number concentrations exceeding 10^6 m^{-3}. It is important to accurately classify the dusty region in this type of case study. In the selected vertical cross section, the WRF-simulated and DPR-retrieved LH have comparable vertical shapes and amplitudes. Both results reflect the structure of the tilted frontal surface, with positive LH above it and negative LH below it. The simulated area-averaged LH profiles show positive heating in the entire column, which is a convective-dominated region, and this feature is not significantly affected by dust. DPR-based LH profiles show stratiform-dominated or convective-dominated shapes, depending on the DPR retrieval product.

Keywords: dust aerosol; frontal system; vertical structure of precipitation; latent heat; GPM; WRF; WRF-Chem

CLC number: P412.27 **Document code:** A

1 Introduction

Mineral dust is the dominant type of atmospheric aerosol by mass in China, contributing ~35% of the total aerosol mass with diameters less than 10 μm[1]. Dust particles originating from the Taklimakan and Gobi deserts because of natural wind erosion and anthropogenic activities are usually driven eastward and southward by westerly atmospheric circulation. During transport, the relatively cold, dry dusty air mass may encounter a warmer, more humid air mass from southeastern China and generate deep convective frontal systems with many clouds and much precipitation. These processes provide ideal testbeds for studying interactions between Asian dust aerosols and clouds[2, 3].

Dust aerosols can affect the properties of clouds and precipitation by different mechanisms at different altitudes (temperatures). At low altitudes and warm temperatures, dust particles coated with soluble pollutants such as sulfate can act as cloud condensation nuclei (CCN) that increase the cloud number concentration and decrease the cloud effective particle radius[4, 5]. Furthermore, they can decrease the coalescence efficiency and thus suppress warm rain processes in both shallow rain[6] and deep convective rain[7, 8]. At high altitudes and cold temperatures, insoluble mineral dust particles can act as effective ice nuclei[9] (IN) that enhance heterogeneous ice formation under warmer temperatures and lower supersaturation compared with that under pristine conditions. This mechanism may increase the precipitation rate at high altitudes[7, 8] and modify the cloud vertical structure. Empirical orthogonal function (EOF) analysis[10] revealed that the first

DOI: 10.52396/JUSTC-2021-0238
JUSTC, **2022**, 52(2): 3

EOF modes of rainfall profiles observed by satellite precipitation radar with and without dust loading for convective and stratiform rain are similar, whereas the second and third EOF modes of stratiform rain profiles embedded in a dust-laden atmosphere are significantly enhanced at high layers above the freezing level. In a complex midlatitude mesoscale convective system, where dust is effectively mixed with clouds, the cloud-top temperature of ice clouds was found to be warmer than that in dry, clean areas[3]. Villanueva et al.[11] found that the dust IN effect increases the probability of ice cloud formation by 5%–10% at midlatitudes under the same temperature, water vapor, and stability conditions. In addition, aerosols can have thermodynamic and dynamic effects owing to latent heat (LH) release[12]. Rosenfeld et al.[13] proposed that the suppression and delay of warm rain by the CCN effect of aerosols may cause more liquid cloud droplets to be elevated to higher altitudes and freeze there. This process can release more LH to invigorate the otherwise suppressed convection. Enhanced condensational heating by ultrafine aerosols in deep convective storms was also found in the Amazon rainforest area[14]. However, this invigoration effect may also vary with aerosol type, as indicated by Zhou et al.[15] and Sun and Zhao[16]. Current satellite retrievals of LH profiles are highly uncertain; therefore, observational studies on the effects of dust on LH are rare.

The study of these processes and mechanisms requires vertical profiles of clouds, precipitation, and LH. Satellite-based precipitation radars provide unique estimations of the vertical distribution of precipitation-sized hydrometeors based on the measured backscattered microwave radiation energy. The effects of dust aerosols on clouds have been studied by analyzing the properties of vertical precipitation profiles[5, 7, 8, 17, 18]. However, these observations can reveal only the combined effect of multiple environmental factors, including the aerosol and meteorological effects, on clouds and precipitation. A cloud-resolving model (CRM) is crucial for explaining the mechanisms of aerosol effects in detail. CRMs such as the Weather Research and Forecasting (WRF) model have been widely used to study the impacts of dust aerosols on precipitation[3, 19].

Most previous studies have focused on dust-related variations in surface rain rate and gave less attention to dust-related variations in rainfall vertical structure, which is closely related to latent heating[20, 21]. CRM simulations of the vertical profiles of multiple types of hydrometeors and LH have seldom been compared with real observations, especially on regional scales. It is even more difficult to directly study the possible impacts of aerosols on LH profiles within storms. Although indirect estimates of LH derived from vertical precipitation profiles have been developed[21–23], very few studies have compared them to CRM results or directly investigated the proposed impacts of aerosols on LH in storms. In addition, interactions between tropical deep convective systems and aerosols have received more attention than storms at midlatitudes and/or high latitudes[24].

In this study, the effects of dust on precipitation and LH in a midlatitude frontal system in China were studied using both satellite observations and WRF simulations. We focused on three aspects: ① the dust-related characteristics of precipitation and LH from the WRF simulation, ② the dust-related characteristics of precipitation and LH from satellite observations, and ③ a comparison of the precipitation and LH profiles from satellite observations and WRF simulations.

2 Data and methods

2.1 Satellite observations of precipitation and latent heating

The surface rain rate and vertical precipitation profile data used in this study were derived from observations by the Global Precipitation Measurement (GPM) satellite's passive microwave imager (GMI) and Dual-Frequency Precipitation Radar (DPR), respectively. The GPM satellite orbits at 407 km above ground in a non-Sun-synchronous orbit from 65°S to 65°N. The GMI surface rain rate product has a swath width of 904 km and horizontal resolution of 8 km × 15 km. The DPR precipitation profile product has a swath width of 245 km, vertical resolution of 125 m, and horizontal resolution of ~5.2 km. The DPR can detect only precipitation particles with a radar reflectivity exceeding ~12 dBz. This limit introduces discrepancies between DPR-observed precipitation profiles and those derived from CRMs, particularly in layers near the rain top.

The LH profile data used in this study were retrieved from the DPR precipitation profile product using a vertical profile heating (VPH) algorithm from the University of Science and Technology of China (USTC)[21] which uses a piecewise linear model to represent the LH at each vertical layer as a function of the vertical gradient of the precipitation rate constrained by air temperature. The original VPH method was developed for retrieving the LH over the Tibetan Plateau. However, the concept also applies to midlatitude storms. Two other DPR-based LH products, the Spectrum Latent Heating[23] (SLH) and Convective Stratiform Heating[22] (CSH) were also used. These two methods are look-up-table (LUT) based methods using key and limited real observations, including rain type, surface rain rate, rain top height, as input to retrieve LH[25, 26].

2.2 Satellite observations of aerosol optical depth

The aerosol optical depth (AOD) is derived from Himawari-8 satellite observations. Advanced Himawari Imager (AHI) observations were used in this study. Himawari-8 is a geostationary weather satellite operated by the Japan Aerospace Exploration Agency (JAXA). The AOD retrieval algorithm[27] used for the JAXA official L2 aerosol product utilizes images from the AHI, which is the primary instrument on Himawari-8, to estimate the AOD for non-cloudy pixels on the same grids as the AHI observations (0.05° spatial resolution, 60°S–65°N, 85°E–25°W across the 180th meridian) every 10 min.

2.3 WRF model simulations

Simulations without dust [no dust, (ND)] and with dust (DS) were conducted using a selected case (see Section 3.1). For the ND simulation, only the WRF model was used, without

DOI: 10.52396/JUSTC-2021-0238
JUSTC, **2022**, 52(2): 3

considering the effects of dust aerosols. For the DS simulation, WRF-Chem was used to obtain the spatial and temporal variations of dust aerosols. The WRF-Chem simulation considered only the dust aerosol process and did not consider other aerosols. Information on the dust aerosol distribution was input to the WRF simulation, and the proposed IN effect was taken into account in the associated ice phase microphysical scheme.

WRF and WRF-Chem V4.0 were used in this study. The model simulation used two nested domains; the inner and outer spatial resolutions were 3 and 9 km, respectively. The model was divided into 50 layers in the vertical direction using the mixed vertical coordinate layering method introduced in V3.9. The inner and outer time resolutions of the model simulation were 15 and 30 s, respectively.

The physical scheme used in the model was configured as follows. Microphysical parameterization was performed using the Thompson scheme[28]; the longwave and shortwave radiation scheme used the RRTMG longwave and shortwave radiation schemes, respectively[29]; the near-surface layer scheme used the Revised MM5[30]; the land surface was parameterized using the Unified Noah scheme[31]; the planetary boundary layer scheme used the YSU scheme[32]; convection was parameterized using the Grell-Freitas ensemble scheme[33], which was applied only in the outer domain, and no convection parameters were set in the inner domain area. The GOCART sand and dust scheme[34] was used in the WRF-Chem simulation. This scheme assumes spherical particles and divides dust particles into five bins according to their sizes.

We output the latent heating rate and precipitation rate profiles, which are not included in the WRF standard output. The following formula is used for the precipitation rate (RR):

$$\mathrm{RR}_x = v_x \times \rho \times \frac{q_x}{\rho'},$$

where x represents for different types of precipitation particles (rain, graupel, snow), v_x is the effective terminal fall speed, ρ is the density of air, ρ' is the density of water, and q_x is the mixing ratio of particle x.

The latent heating rate has already been calculated as the "temperature tendency" (i.e., "tten") in Thompson schemes; therefore, we gather the results and write them to WRF outputs.

In the ND simulation, the number concentration of IN (i.e., N_i, unit: $\mathrm{m^{-3}}$) was

$$N_i = 1000.$$

In the DS simulation, following Demotte et al.[35], the number concentration of IN was rewritten as

$$N_i = 1000 + 5.94 \times 10^{-5} \times (273.16 - T)^{3.33} \times n_{ac}^{0.0264 \times (273.16 - T) + 0.0033} \times \frac{\rho}{\rho_0} \times 1000,$$

where n_{ac} is the number concentration of dust (unit: $\mathrm{m^{-3}}$), T is air temperature (unit: K), ρ is air density (unit: $\mathrm{kg \cdot m^{-3}}$), and $\rho_0 = 1.292\ \mathrm{kg \cdot m^{-3}}$ is the air density under standard conditions. In this study, the original n_{ac} calculated by the Thompson scheme was replaced by the total dust number concentration (the sum of bins 1–5) in the GOCART scheme.

The initial conditions and lateral boundary conditions of the model meteorological driving field are based on the Climate Forecast System Reforecast[36] global reanalysis data of the US National Centers for Environmental Prediction. This product was also used for atmospheric circulation analysis.

3 Results

3.1 General features of atmosphere circulation, precipitation, and aerosol distribution in selected case

At 8:00 UTC on May 3, 2017, the northern part of the study area was dominated by westerly winds on the south side of a strong polar vortex (Fig. 1). The East Asian Trough was located at 100°E–115°E, 38°N–44°N, where the airflow direction changes from northwesterly to southwesterly. The cold, dry airmass with dense dust aerosols (refer to Fig. 2 and Fig. 5) moved from west to east with wind speeds of up to ~20 $\mathrm{m \cdot s^{-1}}$ at 850 hPa. In addition, two warm, humid airflows from south China and north of the West Pacific Subtropical High converged and entered the southern part of the study area. A low-pressure cyclone was centered in the Henan–Hubei region. Southeasterly air flow from the East Ocean transported abundant water vapor to the study area on the east side of the cyclone. These air masses met at 110°E–115°E, 30°N–50°N, forming a strong frontal system with many clouds and much precipitation.

According to GMI measurements at 7:50 UTC on that day (Fig. 2a, GMI width: 780 km), a long, narrow southwest-northeast rain belt extended from 30°N to approximately 45°N; the strongest precipitation occurred in Henan and Hubei provinces. In the middle of the GPM orbit, the DPR (Fig. 2b, DPR width: 240 km) measured the three-dimensional precipitation structure and the associated LH. We divided the GMI precipitation area roughly into three sectors (G1, G2, and G3), where both DPR and GMI observations are available in Sector G2.

In addition, in early May, the terrestrial surface of Mongolia and Inner Mongolia was strongly disturbed by northwest airflow at the bottom of the polar vortex, which resulted in a dense dust storm. According to Himawari-8 observations (Fig. 2c), at 8:00 UTC on May 3, in Inner Mongolia and Gansu (upstream of the frontal system), the maximum AOD was at least 5.0. The dust was transported east by the westerly airflow, causing high AOD in Northeast China, the Korean Peninsula, the Bohai Sea, and the Sea of Japan. This dust storm met the frontal system shown in Figs. 2a and 2b.

Overall, WRF simulations of the horizontal distribution of precipitation and dust (Figs. 2d, 2e, and 2f) are consistent with satellite observations. The WRF-simulated surface precipitation rates near the GPM overpass time are shown in Fig. 2d (WRF-ND) and Fig. 2e (WRF-DS). In Sectors G1 and G2, the WRF simulated rain area, spatial pattern of rain, and surface rain rate amplitude are all similar to those observed by GPM (a quantitative comparison is presented in Section 3.2). The model successfully simulated a long, narrow rain belt north of 35°N, which is consistent with the GPM-observed front line. However, the simulated rain area of the front was

DOI: 10.52396/JUSTC-2021-0238
JUSTC, **2022**, 52(2): 3

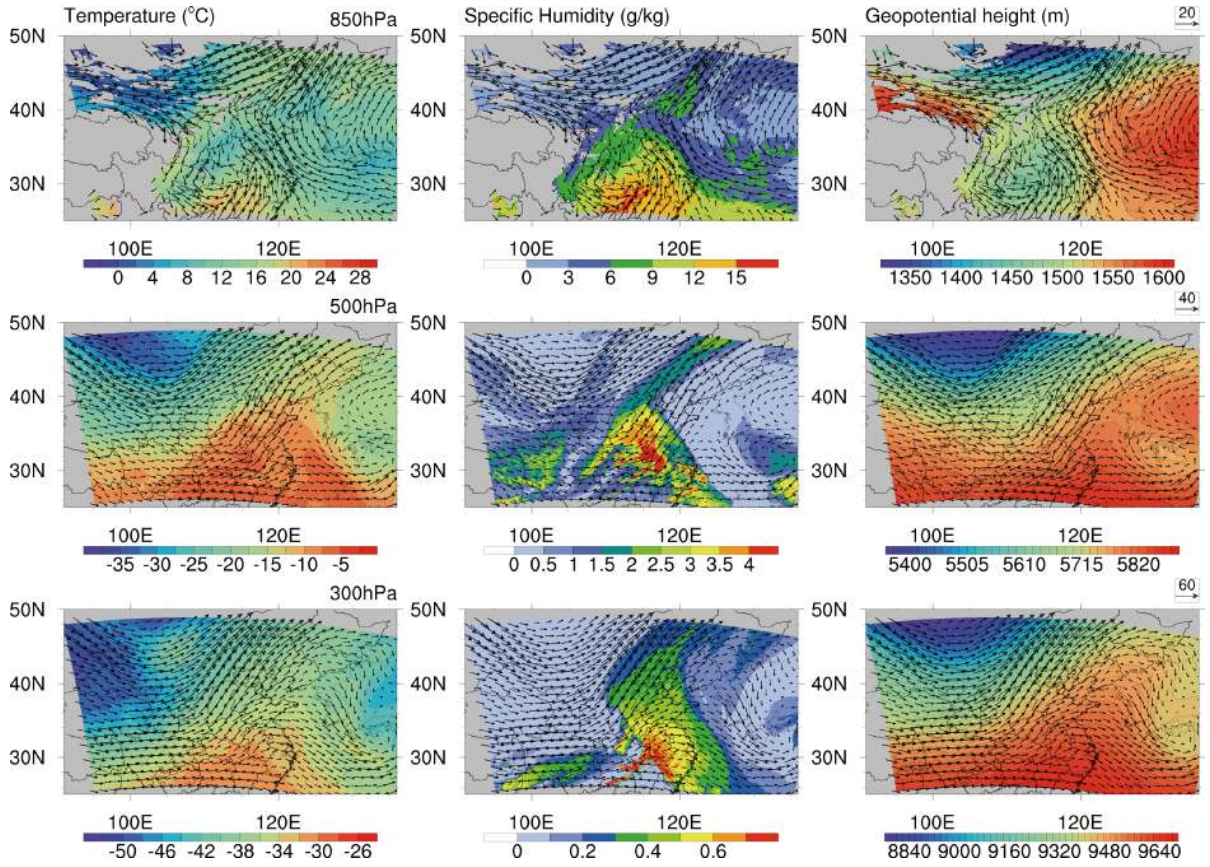

Fig. 1. The spatial pattern of air temperature (left column), specific humidity (central column) and geopotential height (right column) at 850 hPa (top row), 500 hPa (middle row) and 300 hPa (bottom row) at 8:00 UTC on 2017-05-03 derived from Climate Forecast System Reforecast product.

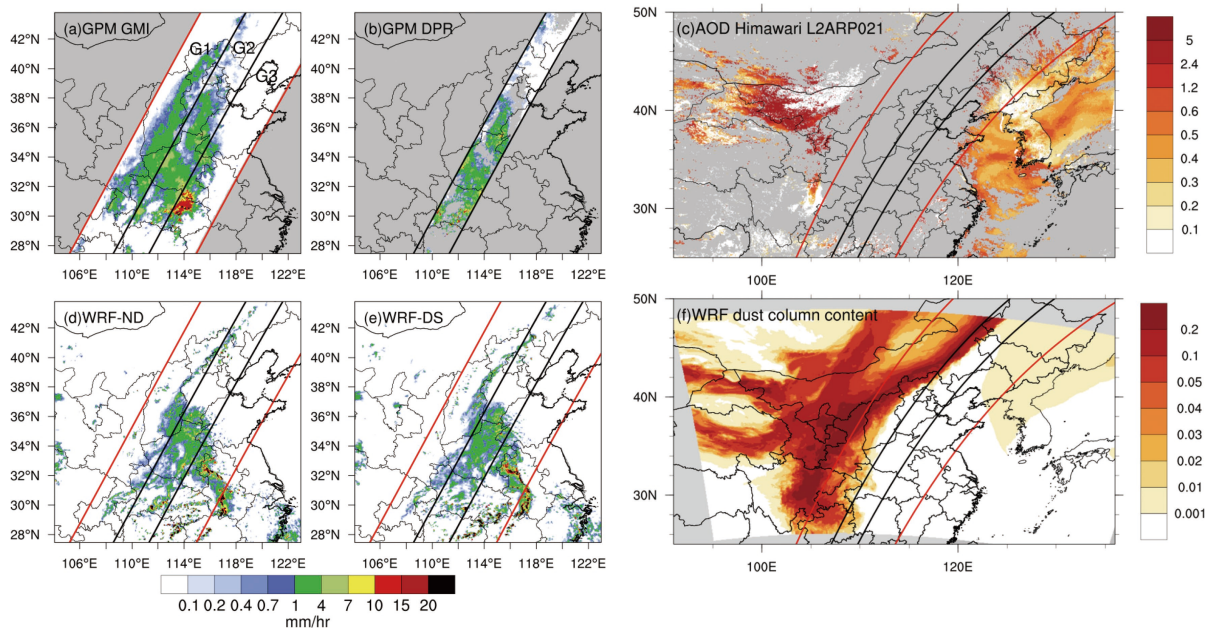

Fig. 2. Satellite observations and model simulations of precipitation and aerosol distribution. (a) GPM GMI observed surface rain rate; (b) GPM DPR observed surface rain rate; (c) Himawari-8 observed aerosol optical depth; (d) WRF simulated surface rain rate without dust; (e) WRF simulated surface rain rate with dust; (f) WRF simulated dust column content.

smaller, and the simulated rain intensity was weaker. In Sector G3, although the WRF model also showed significant precipitation (peak rain rate of >10 mm·h^{-1}), which is consistent with the GPM observation, the spatial pattern of the simulated rain belt is more southeast-oriented, whereas the GPM observation is more northwest-oriented.

In cloudy areas, Himawari cannot identify aerosols. However, the Himawari-observed spatial pattern of the AOD and the WRF-simulated dust distribution suggest that it is very likely that the dust plume did reach the frontal system,

DOI: 10.52396/JUSTC-2021-0238
JUSTC, **2022**, 52(2): 3

particularly in the northwestern part of the GMI swath.

3.2 Comparison of precipitation features in GPM observations and WRF simulations

The surface rain rate derived from the WRF-DS simulation (with a resolution of 3 km) and GMI observations (with a resolution of 5 km) in Sector G1 were compared at scales of 5 km and grid spacings of 0.1°, 0.25°, and 0.5° (Fig. 3). For the 5 km scale, GMI observations were compared to the nearest WRF-DS simulation. At other scales, multiple fine-resolution data inside the cell were averaged to establish coarse-resolution data for comparison. The correlation coefficients R in other sectors are shown in Table 1.

In Sector G1, there is a positive correlation (R = 0.31) in the original satellite field of view. With increasing scale, the positive correlation is enhanced, and R increased to 0.54 for the 0.5° grid. This phenomenon is also found in Sector G2, whereas a much weaker correlation is found in G3 because of

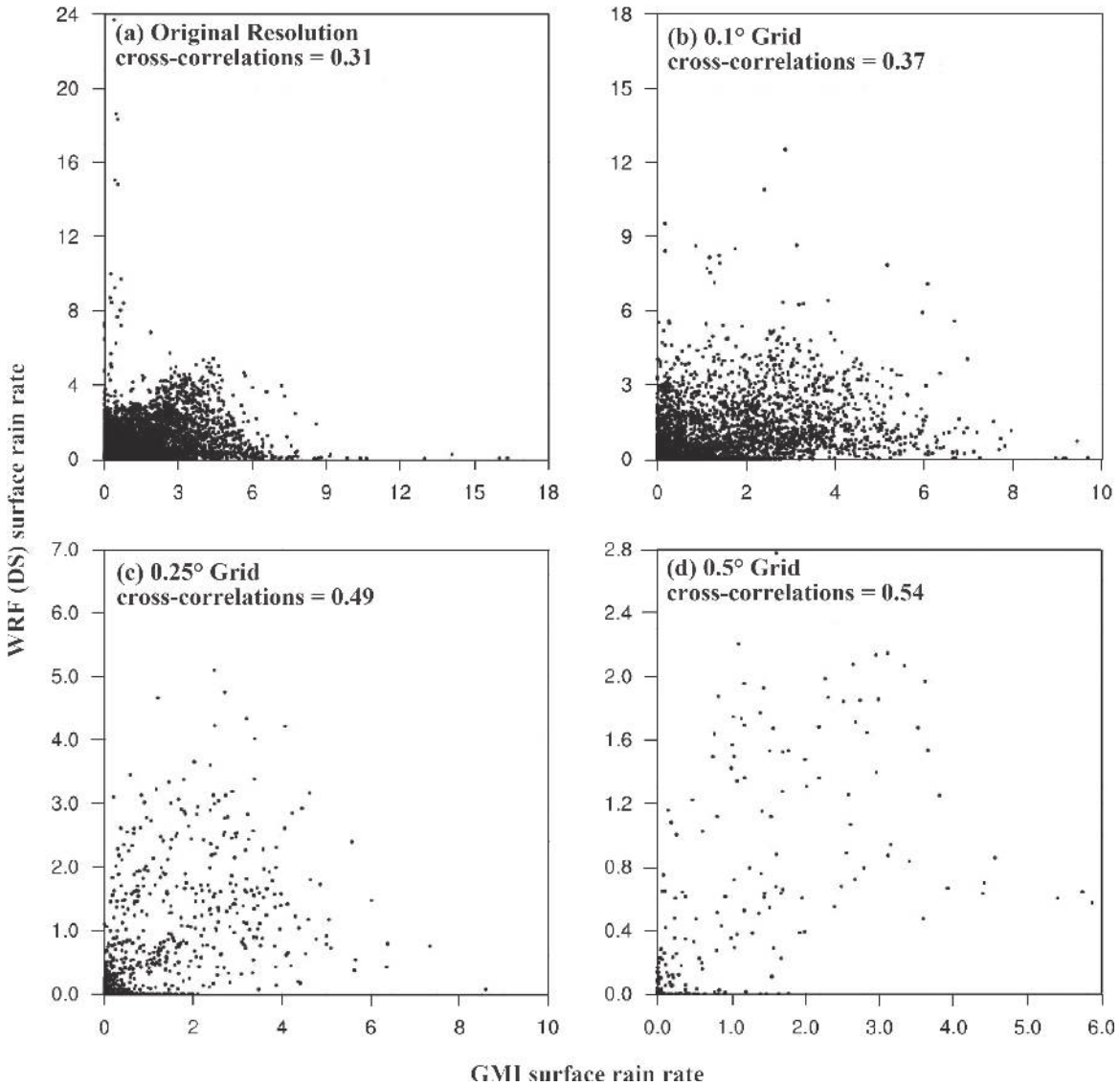

Fig. 3. Scatterplot between GMI observed surface rain rate against WRF simulated surface rain rate in sector G1 at (a) original resolution of GMI; (b) 0.1° grid; (c) 0.25° grid; and (d) 0.5° grid.

Table 1. The correlation coefficients (R) between GMI observed surface rain rate and those simulated by WRF without (ND) and with (DS) dust in sectors G1, G2 and G3 at different horizontal resolution of 5 km, 0.1°, 0.25° and 0.5° grid.

	G1		G2		G3	
	ND	DS	ND	DS	ND	DS
5 km	0.32	0.31	0.22	0.21	0.03	0.00
0.1° grid	0.37	0.37	0.25	0.27	0.01	0.01
0.25° grid	0.52	0.49	0.33	0.35	0.02	0.03
0.5° grid	0.55	0.54	0.60	0.67	0.04	0.03

DOI: 10.52396/JUSTC-2021-0238
JUSTC, **2022**, 52(2): 3

spatial mismatch of the rain areas (Fig. 2e).

In addition, the WRF-ND simulation was also compared to the GMI observations; the results are essentially the same as those for WRF-DS (Table 1). This finding indicates that the inclusion of dust in the WRF simulation, at least in this case, had a weak effect on the consistency of the surface rain rate between the model and satellite data, except in G2, where the DS simulation has a larger R value (0.67) than the ND simulation (0.60) on the 0.5° grid.

In this study, we explicitly output the rain rate in each vertical layer in the WRF simulation. Because Ku-band radar has a minimum measurable rain rate of 0.5 mm·h^{-1}, as stated in the DPR Algorithm Theoretical Basis document[37], we truncated all the WRF-simulated rain rates to less than 0.5 mm·h^{-1} in each layer for the comparison (Fig. 4).

Overall, the WRF area mean (inside the DPR swath) vertical profiles of the rain rate are comparable to those derived from the DPR, as shown in Fig. 4a. In the layers above 4 km, the simulated precipitation rate is significantly higher than that of the DPR. The simulated rain top height (~10.5 km) is approximately 2 km higher than that from the DPR observations. Because we already truncated light rain from the WRF outputs, this discrepancy cannot be completely explained by the sensitivity of the DPR. Instead, it seems that the WRF model (DPR) overestimates (underestimates) rain rates in high layers. In the layers below 4 km, the mean precipitation rates observed by the DPR are higher than those of the model simulation. The mean precipitation rate of the DS simulation in each layer is slightly lower than that of the ND simulation.

To reduce the discrepancies in the absolute intensity and geolocation of rain between the WRF and DPR, we calculated the probability functions for different rain rate bins and vertical altitudes. Fig. 4 shows this joint probability distribution functions (JPDFs) of the height and rain rate derived from DPR observations and the WRF-ND and WRF-DS simulations. Although remarkable differences appear above 4–5 km, as in the mean profiles (Fig. 4a), the JPDF of the DPR is positively correlated (R = 0.77 and 0.83) with the WRF-ND and WRF-DS simulations, respectively. The JPDFs below 4 km of the DPR observations and the two simulations are in good agreement. Fig. 4 also shows that the profile of the 99.5 percentiles of the ND and DS simulations are similar to the DPR observations below ~4.5 km. The consistency between the DPR and WRD-ND is even better than that between the DPR and WRF-DS. Overall, it is encouraging that the JPDFs of the DPR observations and WRF simulations below ~6 km exhibit similar patterns, although the discrepancies in high layers are significant, indicating that both the model simulations and satellite retrievals must be further improved.

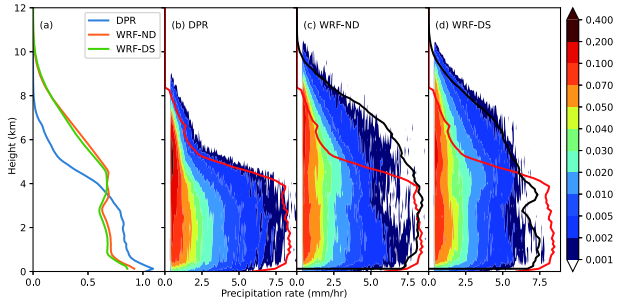

Fig. 4. The intercomparison of rainfall vertical structure between DPR retrievals and WRF simulations. (a) The area means vertical profiles of precipitation rate area. The joint probability function (JPDF) of height and precipitation rate derived from (b) DPR observation, (c) WRF-ND simulation and (d) WRF-DS simulation, where red lines are 99.5 percentiles of DPR observation, and black lines are 99.5 percentiles of WRF simulations (ND, DS, respectively).

3.3 Comparison of clouds, precipitation, and LH with and without dust as additional IN between WRF simulations

The DPR did not observe the entire frontal system, especially on the side directly facing the high dust concentrations (Sector G1). The WRF model yielded a complete characterization of the entire system, and the effects of dust on the system can be directly studied by comparing the DS and ND simulations. Therefore, we first used the WRF simulations to study the effects of dust on clouds and precipitation in the system.

Fig. 5 shows the horizontal distribution of the atmospheric dust column mass density (μg·m^{-2}) simulated by the WRF and the column ice cloud water path (kg·m^{-2}). We made five vertical cross sections along the lines shown in Fig. 5. Here we discuss three of them in detail.

Fig. 6 shows vertical cross sections of water vapor, cloud ice, snowfall, rain rate, and LH simulated by WRF-DS and WRF-ND along line 1, which is perpendicular to the front line (Fig. 5). The wind field is also shown.

The first column shows the WRF-DS simulation, and the brown contour represents the dust column concentration. Figs. 5 and 6 show that the dry, cold northwesterly air flows carrying dust meet the warm, humid southeasterly air flows along the edge of Taihang Mountain. The warm airmass rises over the cold airmass, forming an obvious frontal slope from southeast to northwest. The DS and ND simulations both show significant amounts of cloud ice and snow above the frontal surface, and the cloud bottom height is in excellent agreement with the frontal surface. The WRF-DS results show that the dust extends from 6 to 12 km, providing abundant IN for ice-phase cloud physical processes above the front. However, as the two air flows converged on the front and then moved northwest (see Fig. 8 for analysis), most of the dust particles were distributed only near the front and did not penetrate the warm, humid mass in the southeast (brown con-

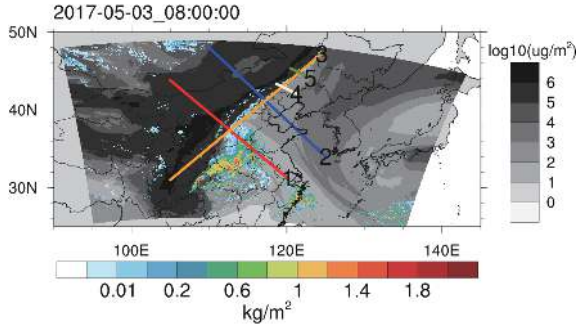

Fig. 5. The dust column density (gray shaded) and ice water path (rainbow shaded) simulated by WRF and five selected lines for making cross-section analysis.

DOI: 10.52396/JUSTC-2021-0238
JUSTC, **2022**, 52(2): 3

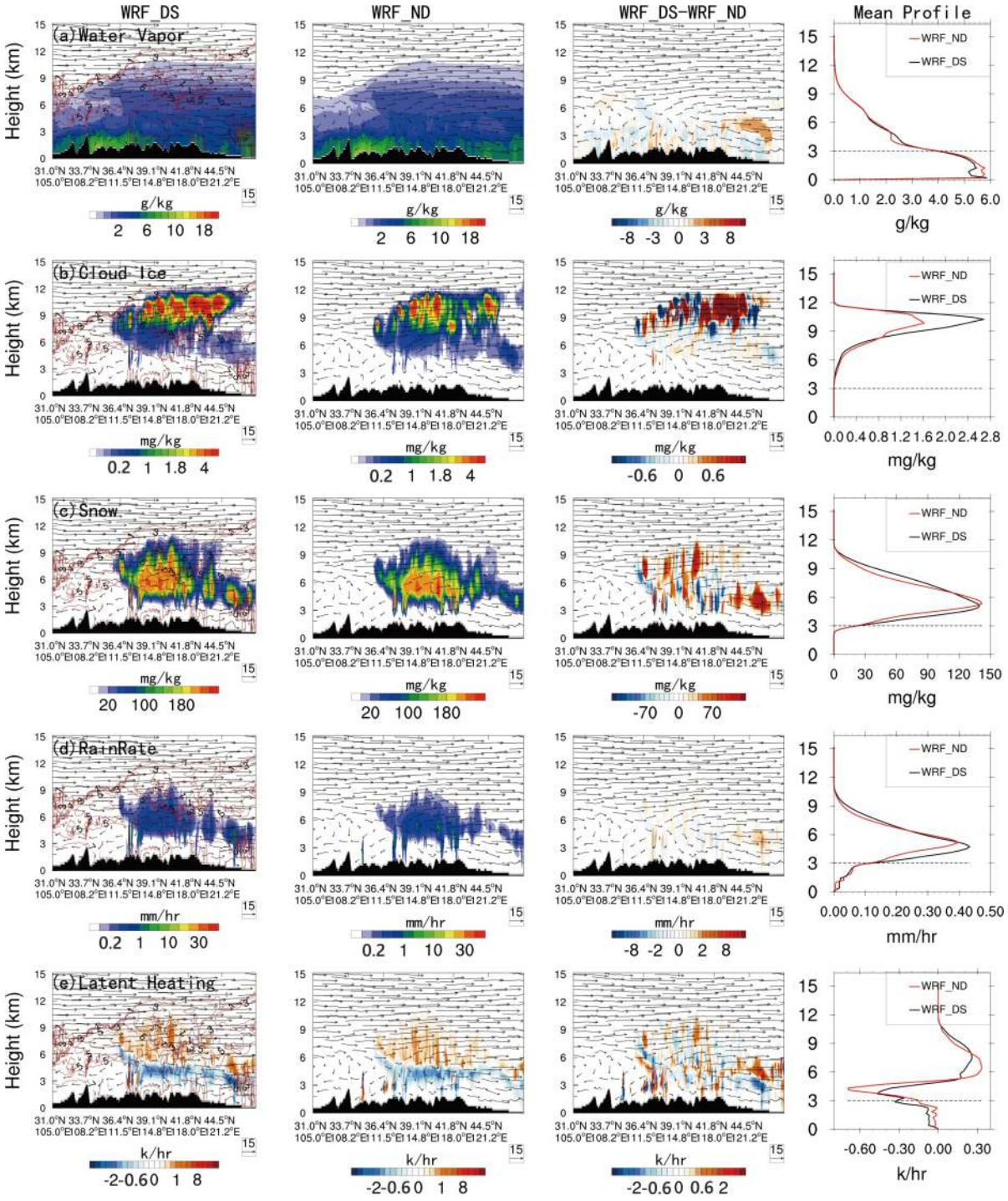

Fig. 6. WRF DS and ND cross sections along line 1 in Fig. 5 (perpendicular to the front line). The first column is from WRF-DS simulation, the second column is from the WRF-ND simulation, and the third column is the difference between these two simulations. The fourth column is the mean profile averaged over the whole cross section. Different rows represent different variables as denoted at top left of every row. Brown contour lines in the 1st column represent dust concentrations. Vectors are wind fields (vertical winds are multiplied by 5).

tour in Fig. 6a), which also limited the dust IN effect to the frontal surface area. In the WRF-ND simulation, although there is no dust, the default IN (number concentration: 1000 m^{-3}) seems sufficient to form cloud ice and snow.

The difference between the WRF-DS and WRF-ND simulations (third column in Fig. 6) shows that in the northwestern part of the region of heavy dust, more cloud ice and snow formed at 4–6 km (the heterogeneous freezing altitude) and released more LH at the same time. The WRF-DS simulation shows significantly enhanced cloud ice, snowfall, and LH above the front. However, on the southeast side of the front, the cloud ice, snowfall, and LH in the DS simulation are all lower than those in the ND simulation. We speculate that because the water vapor content is essentially the same, and the

DOI: 10.52396/JUSTC-2021-0238
JUSTC, **2022**, 52(2): 3

dust in the DS experiment consumes more water vapor in the front area, it weakened cloud formation in the downstream area.

The fourth column in Fig. 6 shows the mean profiles in the entire cross section. The cloud ice, snowfall, and LH profiles from the DS and ND simulations are fairly similar. We therefore conclude that dust may have significantly affected the storm in certain areas of the entire system, but this effect is not remarkable over large areas because of insufficient penetration of the storm by dust.

In another cross section (Fig. 7) perpendicular to the front (along the line 2 in Fig. 5), the dust concentration is very high in the WRF-DS simulation because of the very narrow rain belt embedded in the area of heavy dust. Again, WRF-DS shows greatly enhanced cloud ice, snow, rain, and LH at high altitudes compared to WRF-ND in all the vertical cross section plots and area mean profiles.

Fig. 8 shows vertical cross sections along the front line (line 3 in Fig. 5). In contrast to the large spatial gradient of the dust concentration in Fig. 6, the dust concentration was

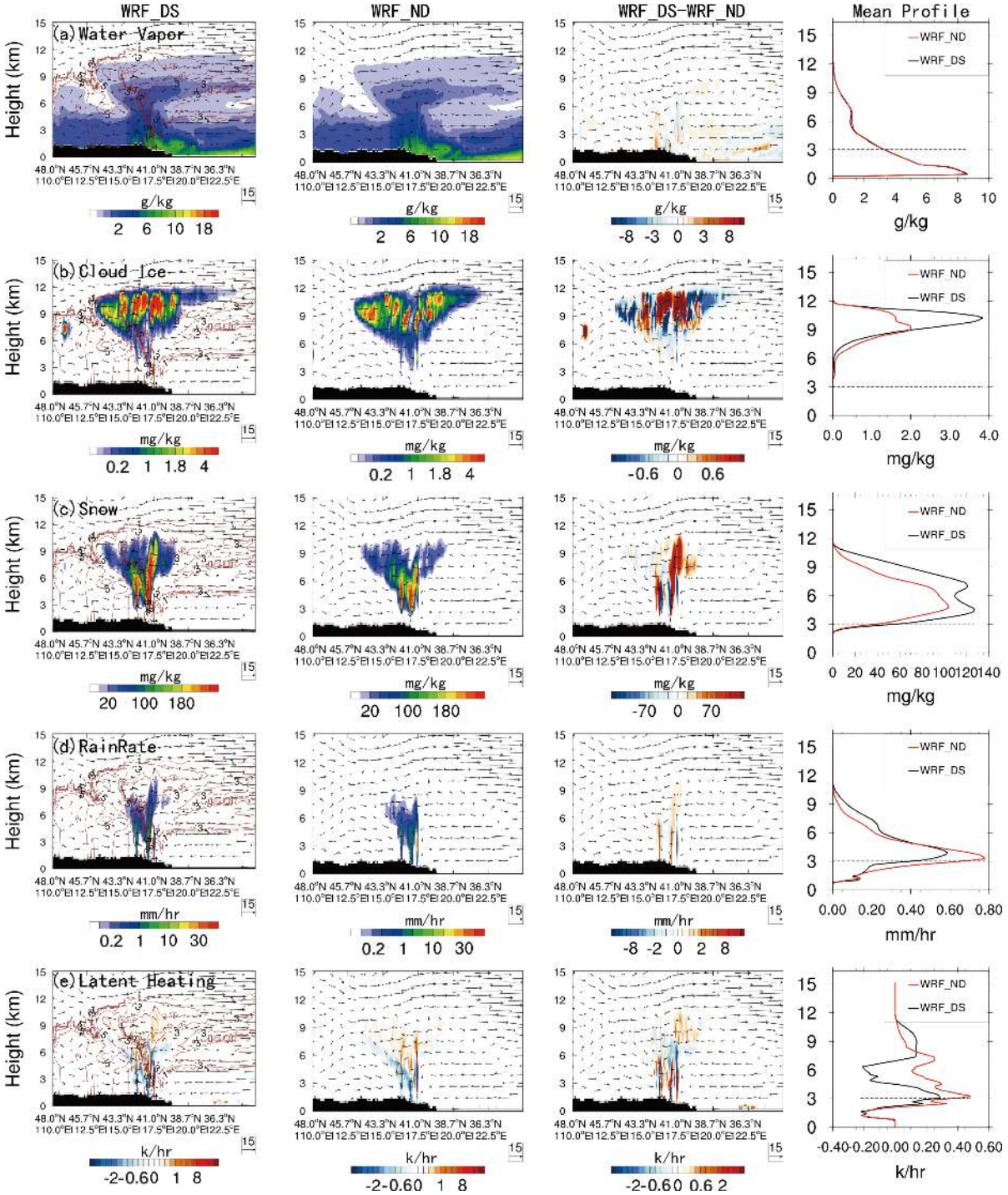

Fig. 7. Same as Fig. 6, but along line 2 in Fig. 5 (perpendicular to the front line).

DOI: 10.52396/JUSTC-2021-0238
JUSTC, **2022**, 52(2): 3

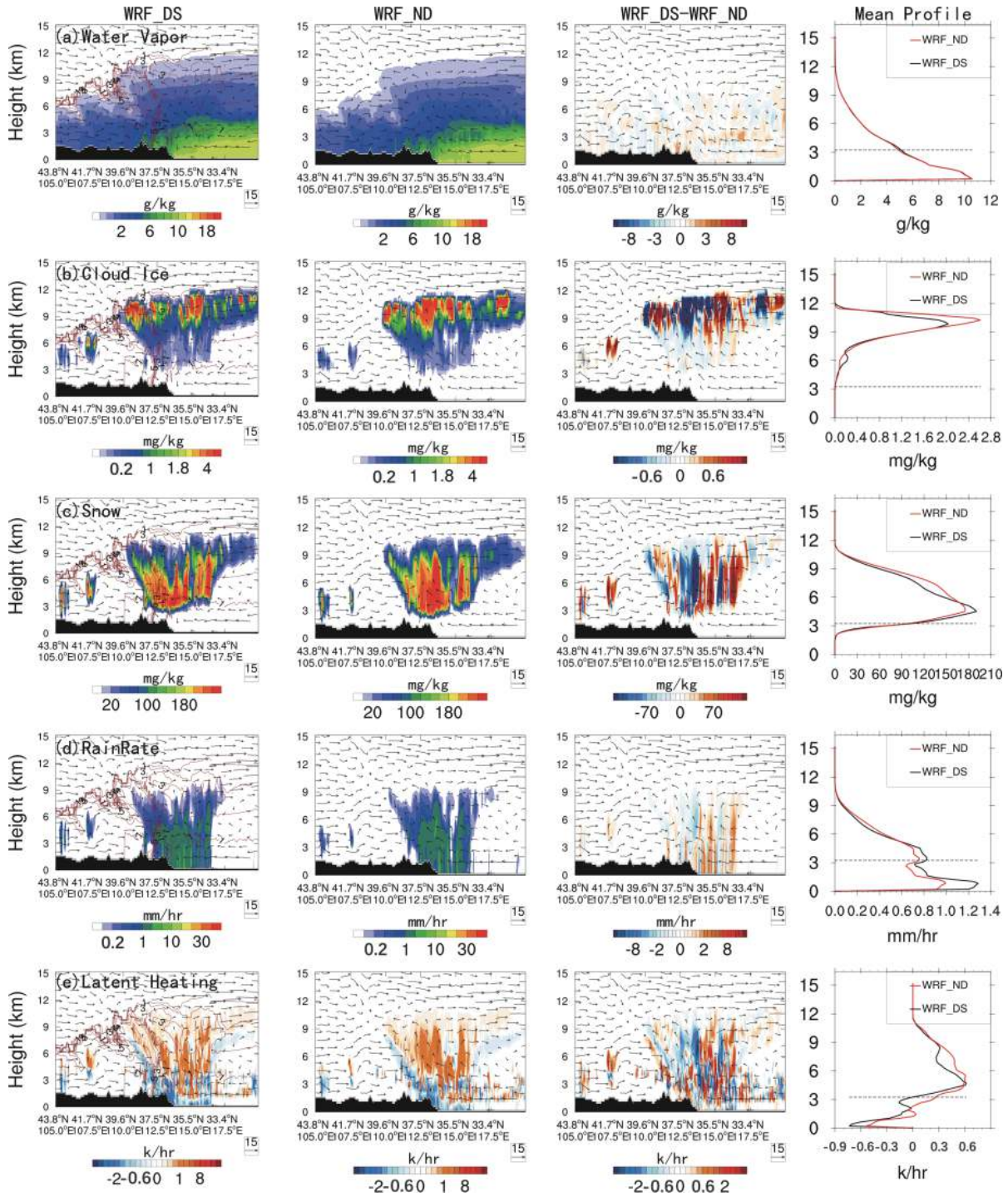

Fig. 8. Same as Fig. 6, but along line 3 in Fig. 5.

high throughout the cross section (the brown contour in Fig. 7a). This cross section along the front does not show an interface between the northwesterly and southeasterly airflows. Instead, strong horizontal winds appear, many stronger than 10 $m \cdot s^{-1}$. Note that in the DS simulation, most cloud-forming areas have high dust contents. The dust was lifted by the wind as it was transported from southwest to northeast, and it extended from near the surface to 12 km.

Although the water vapor (first row) and liquid cloud water (not shown) simulated by WRF-DS and WRF-ND are in good agreement, WRF-DS shows significantly more cloud ice than WRF-ND. This result clearly shows that the dust-induced additional IN enhanced the ice formation by heterogeneous nucleation. The LH profiles simulated by WRF-DS and WRF-ND show a clear boundary at 4–6 km associated with the frontal surface. Above this boundary, updrafts clearly appear, which release LH and heat the atmosphere via condensation, freezing, and sublimation. Below this boundary, downdrafts clearly appear, which cause the absorption of LH and cool the atmosphere via evaporation and melting. Because the dust effect enhances heterogeneous ice nucleation in the WRF-DS simulation, slightly more LH is released above

DOI: 10.52396/JUSTC-2021-0238
JUSTC, **2022**, 52(2): 3

the boundary than in the WRF-ND simulation.

In this cross section, dust affects ice formation in most areas; therefore, the area mean profiles (right column) generally show clear enhancement of cloud ice, snow, and latent heating by dust at high altitudes.

We studied the differences in cloud ice, snow, and LH between the WRF-DS and WRF-ND simulations (DS minus ND) as functions of temperature and number concentration of dust in clouds (Fig. 9) for the region in which the GMI swath and WRF simulation domain overlap, which we believe is the part of the frontal system most strongly affected by dust, as shown in Fig. 2. The results confirm the theoretical understanding of the different mechanisms of ice formation. At temperatures below −38 °C, the homogeneous ice formation mechanisms work equally well in both the DS and ND simulations. That is, the difference (which is somewhat random around zero) does not depend on dust number concentration. At temperatures below −15°C but above −38°C, heterogeneous ice formation dominates, and IN are required. Because the ice number concentration in WRF-ND is equal to 1000 m^{-3}, the WRF-DS simulation does not show significant enhancement when the dust concentration is less than 1000 m^{-3}. With increasing number concentration of dust, the enhancement becomes clear. In particular, when the concentration exceeds 10^6 m^{-3}, the enhancement of cloud ice, snow, and LH increases dramatically. This result demonstrates that the enhancement of ice formation by dust requires a high number concentration.

3.4 Features of latent heating vertical structure observed in GPM DPR retrievals

It is very difficult to directly compare the instantaneous re-

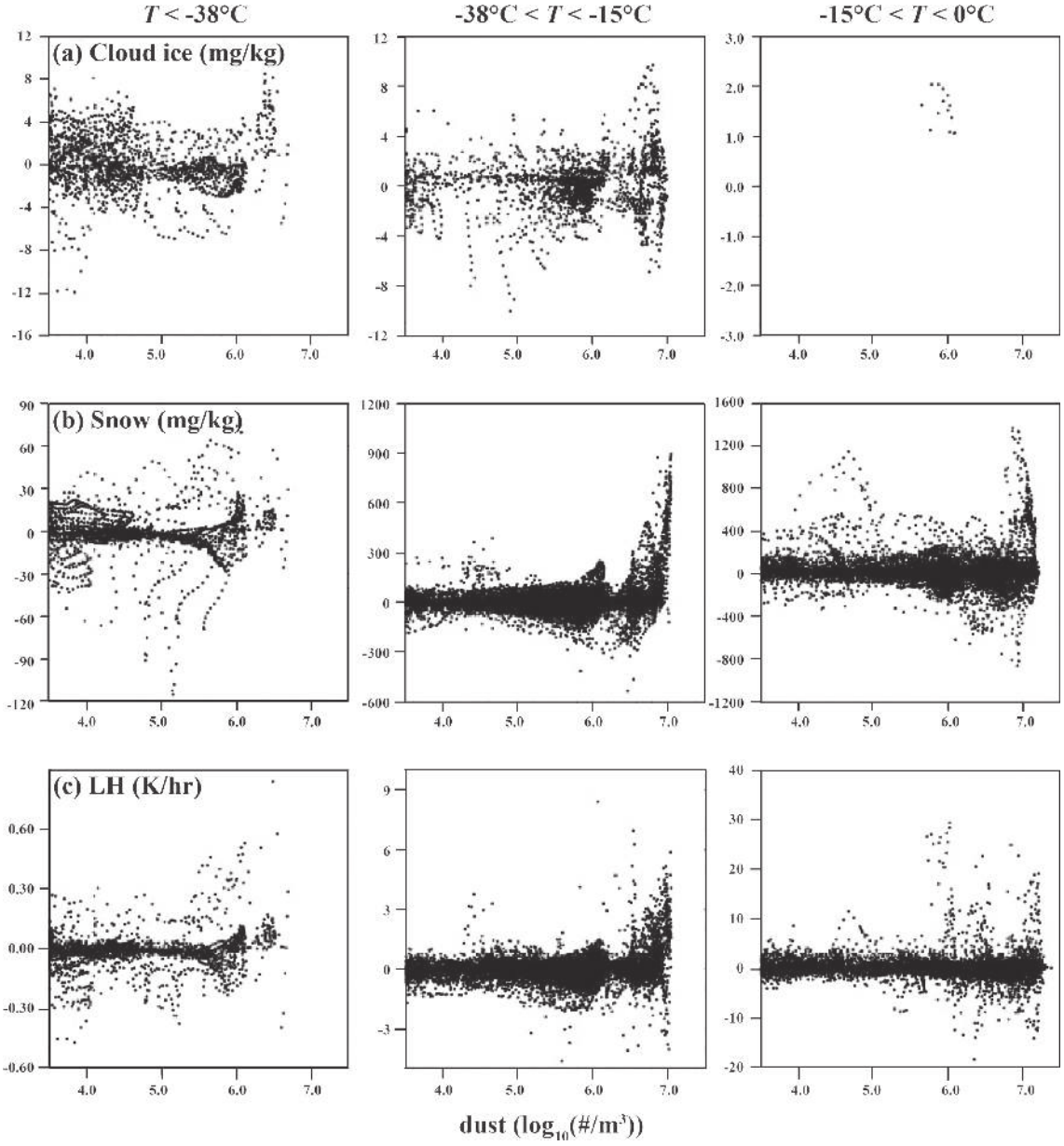

Fig. 9. The difference of cloud ice (up row), snow (mid row) and latent heating (bottom row) between WRF-DS and WRF-ND at temperature colder than –38 ℃, –38 – –15 ℃ and warmer than –15 ℃ as functions of dust number concentration.

DOI: 10.52396/JUSTC-2021-0238
JUSTC, **2022**, 52(2): 3

trieval of LH by DPR with a model simulation at a certain vertical cross section. Slight discrepancies in the location of rain between the DPR observation and WRF simulation make such comparisons impossible. After careful searching, we found two relatively comparable cases, as shown in Fig. 10 (along line 4 in Fig. 5) and Fig. 11 (along line 5 in Fig. 5). In both figures, the first row shows the vertical cross section of the precipitation rates of the DPR, WRF-ND, and WRF-DS; the second row shows the LH retrieved by SLH, CSH, and VPH; and the third row shows the LH simulated by WRF-ND and WRF-DS.

As shown in Fig. 10, the DPR observed a weak precipitation system with a rain top surface tilted to the west. The rain top height was 3–5.5 km, and the peak precipitation rate of approximately 0.7 mm·h^{-1} occurred at an altitude of ~3 km. Both WRF-ND and WRF-DS simulated precipitation systems in similar locations. The WRF-ND simulation shows a much higher rain rate. The WRF-DS simulation is closer to the DPR observation, with a rain top height of ~7 km and peak precipitation rate of 1.5 mm·h^{-1} at an altitude of ~4 km.

For the LH, the DPR VPH and SLH products both show a clear frontal surface tilted from east to west, which is associated with positive heating above and negative cooling below it. In the vertical cross sections of the LH simulated by WRD-DS and WRF-ND, tilted surfaces dividing positive and negative LH are also very clear. In the CSH results, the boundary between positive and negative LH is relatively flat, without significant tilted structure. The reason is most likely that the CSH algorithm classified these samples as stratiform rains, which have similar boundaries near the freezing level.

However, the CSH product shows more LH above an altitude of 6 km, which is closer to the WRF-DS simulations. In the area mean LH profiles in Fig. 10i, the mean LH profile

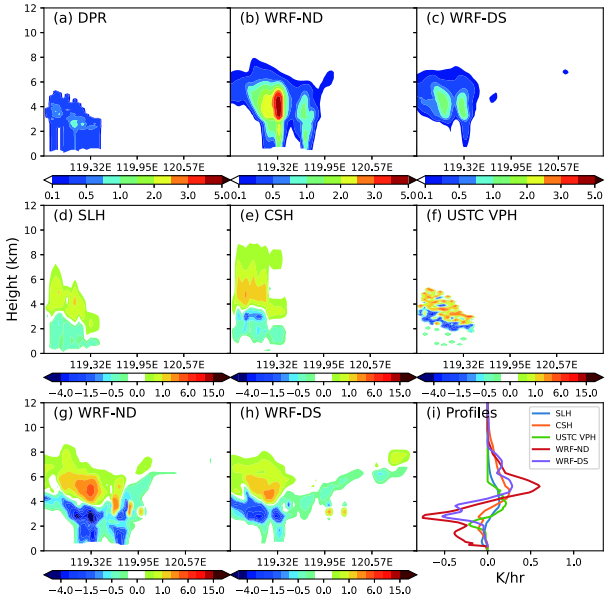

Fig. 10. DPR vs. WRF cross section along line 4 in Fig. 5. (a) DPR precipitation rate; (b) WRF-ND precipitation rate; (c) WRF-DS precipitation rate; (d) SLH latent heating product; (e) CSH latent heating product; (f) USTC-VPH latent heating product; (g) WRF-ND latent heating; (h) WRF-DS latent heating;(i) mean latent heating profile of SLH, CSH, USTC-VPH, WRF-ND and WRF-DS.

from CSH (orange curve) is very similar to those of WRF-DS above 4 km. In the layers at 2–4 km, WRF-DS shows stronger cooling than all the DPR-based LH products.

As shown in Fig. 11, the DPR observed two columnar precipitation systems. Figs. 11b and 11c show that WRF-ND and WRF-DS, respectively, simulated two similar precipitation systems. WRF-DS shows a higher precipitation rate in the precipitation column on the right than WRF-ND. Figs. 11d, 11e, and 11f show that the three DPR LH products all indicate that the precipitation system on the left was a frontal precipitation system. This result is consistent with the WRF simulation results in Figs. 11g and 11h. However, the three DPR LH products show different features for the precipitation system on the right. The SLH and CSH LH products show that the precipitation system on the right was convectively heated, and the LH was positive throughout the vertical column. The VPH product shows that the LH in this precipitation system was positive above and negative below ~2.4 km. The results of both the WRF-ND and WRF-DS simulations were similar to those of VPH retrieval; that is, the precipitation system on the right has positive (negative) LH above (below) 2.4 km. However, WRF-DS shows stronger latent heating above 2.4 km than WRF-ND, indicating that dust enhanced the latent heating. This result is also shown in Fig. 11i.

Finally, Fig. 12 compares the area-averaged vertical profiles of LH retrieved by SLH, CSH, and VPH and simulated by WRF-ND and WRF-DS. The LH results from SLH (black) and CSH (red) show typical top-heavy profiles, with positive (negative) LH above (below) 4 km. This result implies that the SLH and CSH algorithms classified most rainfall as stratiform rain[38]. However, the LH profiles of VPH (green) and the WRF simulations (orange and blue) show positive heating in almost the entire column, except for the layers very close to the surface (below 1 km), indicating convective-dominant precipitation. In particular, the VPH LH result clearly shows a bottom-heavy profile.

The CSH algorithm shows a much larger LH (by a factor of

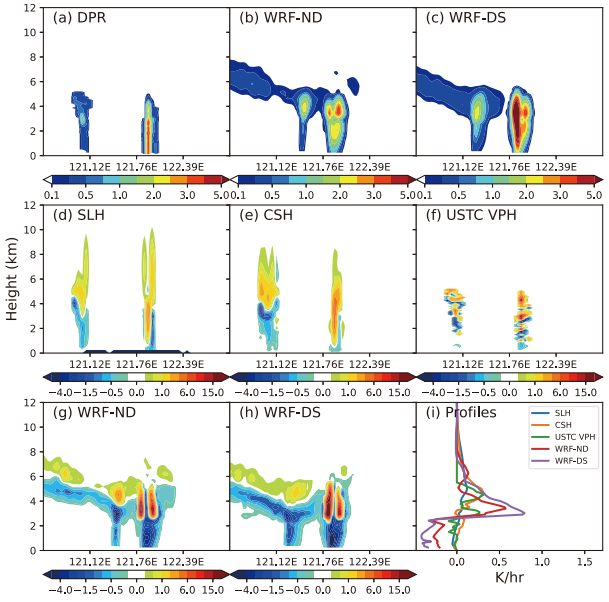

Fig. 11. Same as Fig. 10, but along line 5 in Fig. 5.

DOI: 10.52396/JUSTC-2021-0238
JUSTC, **2022**, 52(2): 3

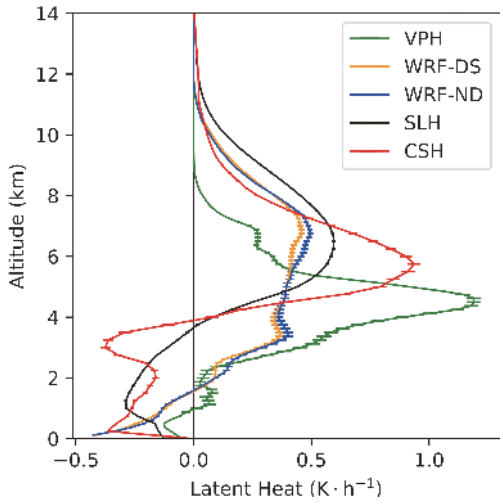

Fig. 12. Average vertical profile of latent heat retrieved by JAXA SLH, NASA CSH, USTC VPH, WRF-ND and WRF-DS in the whole study area.

approximately 2) at 5–7 km compared to the other results. The SLH shows latent heating closer to the model results at 5–7 km, whereas the VPH results is closer to that of the SLH algorithm but 0.1–0.2 K·h^{-1} smaller. The VPH heating has a strong peak at 3.5–5 km (up to 1.2 K·h^{-1}), which is inconsistent with the results of the other four products, indicating problems with the VPH product in the inversion near the freezing layer. However, below 3.5 km, the VPH LH is very close to the model-simulated LH.

Because of the lack of LH retrieval above the rain top height, the VPH LH above 6 km is much smaller than that of the other LH products. In addition, its maximum LH height is only 4.5 km, whereas those of the SLH and CSH algorithms are 6.5 and 6.0 km, respectively, which are similar to those simulated by WRF.

Note the LHs simulated by WRF-DS and WRF-ND are very similar. The reason is that dust affected only a small area of rain, as described above, and thus the impacts of dust on LH become unclear when samples from a large area are averaged.

4 Discussion and conclusion

A case study on the features of clouds, precipitation, and LH in a midlatitude frontal system mixed with a strong dust storm was conducted using GPM satellite observations and WRF modeling results. An analysis of atmospheric circulation revealed that the dust storm mixed only with the narrow northwest edge of the frontal system but did not penetrate deeply into the system. Consequently, the expected dust IN effect was significant only in small areas where clouds were clearly mixed with dust. The averaged features of large areas did not show most of the effects of dust IN. This result demonstrates the importance of accurately classifying areas of heavy dust in this type of case study.

We compared the results of WRF simulations with GPM GMI observations. The WRF simulations correctly captured the spatial distribution of the surface rain rate, with a correlation coefficient R of 0.31 at the original resolution of the GMI footprint; R increased to 0.55 with increasing average scale. Then we compared the WRF-simulated rainfall profiles with GPM DPR observations. Although the mean rain rate profiles from the DPR observations and WRF simulation showed significant discrepancies (which are attributed in part to the detection threshold of the DPR), the probability distributions of the rain rate at layers below 6 km were in good agreement with correlation coefficients R of 0.77–0.83. These results indicate that dust did not significantly affect the output of the WRF simulations.

A significant dust IN effect, specifically, enhanced heterogeneous ice formation, was found in selected vertical cross sections polluted by the dust plume. The WRF simulation with dust clearly showed higher cloud ice, snow, and precipitation rate at high altitudes compared to the dust-free WRF simulation. The associated latent heating rate was also enhanced in the WRF simulation with dust. However, in vertical cross sections far from the dust plume, the dust IN effect did not appear. In addition, the WRF simulation results showed that the dust IN effect appears only at temperatures between −15°C and −38°C. This result confirmed that dust can act as IN to cause ice formation at warmer temperatures than under pristine conditions.

The DPR-based instantaneous retrieval of the rain rate and latent heating in two selected vertical cross sections were also compared with the WRF simulations. The SLH, CSH, and VPH results were presented. Overall, the three LH products showed LH vertical structures with patterns similar to those of the WRF simulations. However, discrepancies appeared among them, particularly in the representation of the tilted structure of the frontal surface and in the sign of the LH in low layers near the surface. The VPH algorithm, which averages over the entire study area, showed positive LH in the entire column, with significant underestimation of the LH at altitudes above 6.5 km, but its results were similar to those of the WRF simulations for lower layers. The SLH and CSH both showed classical stratiform-type LH profiles with significant negative LH (cooling) below 4 km, which did not appear in the WRF simulations. Again, when the results were averaged over this large area, the LH profiles showed no remarkable dust IN effect.

Multiple hypotheses have been proposed to explain the mechanisms by which aerosols affect precipitation and associated LH release. These hypotheses are very hard to confirm by observations because of complex meteorological phenomena that may obscure the effects[39]. Our study confirmed and demonstrated this fact by detailed analysis of results from GPM observations and WRF simulations. Multiple difficulties must be overcome in observational studies.

First, for a particular observed storm, it is hard to identify the extent to which the storm is mixed with aerosols and the exact location of dusty areas. Without this information (for example, when the expected aerosol effect is studied using all samples, both dusty and dust-free), the results may be inconclusive. In this study, the WRF simulations showed a significant dust IN effect only in the very narrow area of the dust plume that mixed with the frontal system (Figs. 6, 7, 8). Enhanced heterogeneous ice nucleation was not observed in areas even slightly distant from the dust plume. Of course,

DOI: 10.52396/JUSTC-2021-0238
JUSTC, **2022**, 52(2): 3

this may also be due to certain meteorological conditions; for example, the strong southeast wind may have stopped the spread of dust from the northwest.

Second, we note that the performance of the observing tools currently used to study dust effects on clouds and precipitation is quite poor. A large bottleneck exists for passive microwave remote sensing of precipitation over land, as its signal source depends strongly on ice-scattering signals. However, the connection between ice water content and surface rain rate is actually weak considering high non-precipitating clouds and warm raining clouds. The effects of dust on surface rain rate may not be strong enough to be detected by passive microwave remote sensing because of its low accuracy. The first limitation of active precipitation radar is its narrow swath width (~240 km for the GPM DPR). It can observe only a small part of a mesoscale convective system and may miss important information on dust-cloud interactions. In addition, because of its detection threshold (~12 dBz), the DPR missed many small ice particles in the upper layer of precipitating clouds. These particles are most likely to be affected by dust. In layers near the surface, the radar signals are contaminated by strong surface echo, and thus the rain rate retrievals are not sufficiently reliable to represent the impacts of aerosols. The uncertainties of satellite-retrieved LH are even larger than those of rain rate. As we found in this study, the results of the three GPM DPR LH products showed different features. Therefore, it is even harder to use current satellite LH products to study the impacts of aerosols on LH profiles.

Third, we considered only a simple dust-related modification of the number concentration of IN in the microphysical scheme of the WRF simulations. However, actual dust could also act as CCN, affecting the warm rain process and introducing more complicated variations in both rain rate and LH. In this study, because we focused on the IN effect, we ignored the CCN effect. The impact of doing so was not evaluated.

This study also yielded some encouraging results. It clearly showed that dust can indeed enhance ice cloud, snow, precipitation, and LH if it is really mixed with the cloud. The WRF-simulated vertical profiles of rain rate and LH were in reasonable agreement with state-of-the-art satellite retrievals. In addition, multiple GPM-DPR-based LH products showed potential for representing the detailed vertical structure of LH within a storm.

Acknowledgements

This work is supported by the National Key Research and Development Program of China (Grant No. 2017YFC1501402), the National Natural Science Foundation of China (Grant Nos. 41830104, 41375148, 41675022), Belmont Forum and JPI Climate Collaborative Research Action with NSFC (Grant No. 41661144007), the "Hundred Talents Program" of the Chinese Academy of Sciences, and the Jiangsu Provincial 2011 Program (Collaborative Innovation Center of Climate Change).

Conflict of interest

The authors declare that they have no conflict of interest.

Biographies

Renjun Zhou is an associate professor at the School of Earth and Space Sciences (ESS), University of Science and Technology of China (USTC). Admitted to ESS in 1995 as an undergraduate majoring in Atmospheric Sciences with a double major in Electronic Engineering, he finished his undergraduate, master and doctoral studies in ESS, and stayed in the school as a faculty member after graduation. He also went to the City University of Hong Kong and Georgia Institute of Technology as a visiting scholar. His research mainly involves numerical modeling of weather and climate and the development of applications in the field of geosciences. He has been PIs for many scientific research projects such as the National Natural Science Foundation of China, and has published more than 40 academic papers in domestic and foreign journals. He also has many years of experience in the software and hardware development, and has carried out a lot of outreaching cooperation with industries in the fields of meteorology, earthquake, environmental protection, electric power, etc. Website: https://ess.ustc.edu.cn/faculties/detail-144.html.

Rui Li received his PhD degree from the University of Science and Technology of China (USTC) in 2005. Before he joined the School of Earth and Space Sciences (ESS) of USTC in 2013, he was a full research scientist in the State University of New York. He was honored as the "Professor of Hundred-Talent Program of Chinese Academy of Sciences" and the "Specially Recruited Experts of Anhui Province in China" in 2013. He now serves as a full professor and deputy dean of ESS USTC; the professor of the State Key Laboratory of Fire Science; the adjunct professor of University of Quebec in Abitibi, Canada; the member of China National Committee for WMO World Weather Research Programee (WWRP); the member of China National Committee for International Association of Meteorology and Atmospheric Sciences (IAMAS); the member of China National Administry Committee on Teaching Atmospheric Science in Higher Education; and the council member of the Anhui Meteorology Society. His research has been focusing on the water cycle and energy balance processes in the Earth's climate system, the development of advanced satellite remote sensing methods and datasets and their application in climate system research. Website: https://ess.ustc.edu.cn/faculties/detail-58.html.

References

[1] Boucher O, Randall D, Artaxo P, et al. Clouds and Aerosols. In: Climate Change 2013: The Physical Science Basis. Working Group I Contribution to the Fifth Assessment Report of the Intergovernmental Panel on Climate Change. Cambridge, UK: Cambridge University Press, 2013: 571 – 658.

[2] Huang J, Minnis P, Lin B, et al. Possible influences of Asian dust aerosols on cloud properties and radiative forcing observed from MODIS and CERES. *Geophysical Research Letters,* **2006**, *33* (6): L06824.

[3] Li R, Dong X, Guo J, et al. The implications of dust ice nuclei effect on cloud top temperature in a complex mesoscale convective system. *Scientific Reports,* **2017**, *7* (1): 13826.

[4] Kaufman Y J, Koren I, Remer L A, et al. The effect of smoke, dust, and pollution aerosol on shallow cloud development over the Atlantic Ocean. *Proceedings of the National Academy of Sciences,* **2005**, *102* (32): 11207–11212.

[5] Li R, Min Q-L, Harrison L C. A case study: The indirect aerosol effects of mineral dust on warm clouds. *Journal of the Atmospheric Sciences,* **2010**, *67* (3): 805–816.

[6] Rosenfeld D, Rudich Y, Lahav R. Desert dust suppressing precipitation: A possible desertification feedback loop. *Proceedings of the National Academy of Sciences,* **2001**, *98* (11): 5975–5980.

[7] Min Q-L, Li R, Lin B, et al. Evidence of mineral dust altering cloud microphysics and precipitation. *Atmospheric Chemistry and Physics,* **2009**, *9* (9): 3223–3231.

DOI: 10.52396/JUSTC-2021-0238
JUSTC, **2022**, 52(2): 3

[8] Li R, Min Q-L. Impacts of mineral dust on the vertical structure of precipitation. *Journal of Geophysical Research,* **2010**, *115*: 09203.
[9] Schaefer V J. The detection of ice nuclei in the free atmosphere. *Journal of Atmospheric Sciences,* **1949**, *6* (4): 283–285.
[10] Dong X, Li R, Wang Y, et al. Potential impacts of Sahara dust aerosol on rainfall vertical structure over the Atlantic Ocean as identified from EOF analysis. *Journal of Geophysical Research: Atmospheres,* **2018**, *123* (16): 8850–8868.
[11] Villanueva D, Heinold B, Seifert P, et al. The day-to-day co-variability between mineral dust and cloud glaciation: A proxy for heterogeneous freezing. *Atmos. Chem. Phys.,* **2020**, *20* (4): 2177–2199.
[12] Zhao C, Lin Y, Wu F, et al. Enlarging rainfall area of tropical cyclones by atmospheric aerosols. *Geophysical Research Letters,* **2018**, *45* (16): 8604–8611.
[13] Rosenfeld D, Lohmann U, Raga G B, et al. Flood or drought: How do aerosols affect precipitation? *Science,* **2008**, *321* (5894): 1309–1313.
[14] Fan J, Rosenfeld D, Zhang Y, et al. Substantial convection and precipitation enhancements by ultrafine aerosol particles. *Science,* **2018**, *359* (6374): 411–418.
[15] Zhou S, Yang J, Wang W-C, et al. An observational study of the effects of aerosols on diurnal variation of heavy rainfall and associated clouds over Beijing–Tianjin–Hebei. *Atmos. Chem. Phys.,* **2020**, *20*: 5211–5229.
[16] Sun Y, Zhao C. Distinct impacts on precipitation by aerosol radiative effect over three different megacity regions of eastern China. *Atmos. Chem. Phys.,* **2021**, *21*: 16555–16574.
[17] Rosenfeld D. TRMM observed first direct evidence of smoke from forest fires inhibiting rainfall. *Geophysical Research Letters,* **1999**, *26* (20): 3105–3108.
[18] Guo J, Liu H, Li Z, et al. Aerosol-induced changes in the vertical structure of precipitation: A perspective of TRMM precipitation radar. *Atmos. Chem. Phys.,* **2018**, *18* (18): 13329–13343.
[19] Naeger A. Impact of dust aerosols on precipitation associated with atmospheric rivers using WRF-Chem simulations. *Results in Physics,* **2018**, *10*: 217–221.
[20] Li R, Min Q, Fu Y. 1997/98 El Niño-induced changes in rainfall vertical structure in the East Pacific. *Journal of Climate,* **2011**, *24* (24): 6373–6391.
[21] Li R, Shao W, Guo J, et al. A simplified algorithm to estimate latent heating rate using vertical rainfall profiles over the Tibetan Plateau. *Journal of Geophysical Research: Atmospheres,* **2019**, *124* (2): 942–963.
[22] Tao W-K, Lang S, Olson W S, et al. Retrieved vertical profiles of latent heat release using TRMM rainfall products for February 1998. *Journal of Applied Meteorology,* **2001**, *40* (6): 957–982.
[23] Shige S, Takayabu Y N, Tao W-K, et al. Spectral retrieval of latent heating profiles from TRMM PR data. Part I: Development of a model-based algorithm. *Journal of Applied Meteorology,* **2004**, *43* (8): 1095–1113.
[24] Fan J, Leung L R, Rosenfeld D, et al. Microphysical effects determine macrophysical response for aerosol impacts on deep convective clouds. *Proceedings of the National Academy of Sciences,* **2013**, *110* (48): E4581–E4590.
[25] Tao W-K, Smith E A, Adler R F, et al. Retrieval of latent heating from TRMM measurements. *Bulletin of the American Meteorological Society,* **2006**, *87* (11): 1555–1572.
[26] Tao W-K, Houze R Jr, Smith E A. The fourth TRMM latent heating workshop. *Bulletin of the American Meteorological Society,* **2007**, *88*: 1255–1259.
[27] Yoshida M, Kikuchi M, Nagao T M, et al. Common retrieval of aerosol properties for imaging satellite sensors. *Journal of the Meteorological Society of Japan. Ser. II,* **2018**, *96B*: 193–209.
[28] Thompson G, Field P R, Rasmussen R M, et al. Explicit forecasts of winter precipitation using an improved bulk microphysics scheme. Part II: Implementation of a new snow parameterization. *Monthly Weather Review,* **2008**, *136* (12): 5095–5115.
[29] Iacono M J, Delamere J S, Mlawer E J, et al. Radiative forcing by long-lived greenhouse gases: Calculations with the AER radiative transfer models. *Journal of Geophysical Research: Atmospheres,* **2008**, *113*: D13103.
[30] Jiménez P A, Dudhia J, González-Rouco J F, et al. A revised scheme for the WRF surface layer formulation. *Monthly Weather Review,* **2012**, *140* (3): 898–918.
[31] Tewari M, Chen F, Wang W, et al. Implementation and verification of the unified Noah land surface model in the WRF model (Formerly Paper Number 17.5). In: 20th Conference on Weather Analysis and Forecasting/16th Conference on Numerical Weather Prediction. Seattle, WA: American Meteorological Society, 2004: 11-15.
[32] Hong S-Y, Noh Y, Dudhia J. A new vertical diffusion package with an explicit treatment of entrainment processes. *Monthly Weather Review,* **2006**, *134* (9): 2318–2341.
[33] Grell G A, Freitas S R. A scale and aerosol aware stochastic convective parameterization for weather and air quality modeling. *Atmos. Chem. Phys.,* **2014**, *14* (10): 5233–5250.
[34] Ginoux P, Chin M, Tegen I, et al. Sources and distributions of dust aerosols simulated with the GOCART model. *Journal of Geophysical Research: Atmospheres,* **2001**, *106* (D17): 20255–20273.
[35] Demott P J, Prenni A J, Liu X, et al. Predicting global atmospheric ice nuclei distributions and their impacts on climate. *Proceedings of the National Academy of Sciences,* **2010**, *107* (25): 11217–11222.
[36] Saha S, Moorthi S, Wu X, et al. The NCEP Climate Forecast System Version 2. *Journal of Climate,* **2014**, *27* (6): 2185–2208.
[37] Iguchi T, Seto S, Meneghini R, et al. GPM/DPR Level-2 algorithm theoretical basis document. Washington, DC: NASA, 2019.
[38] Houze R A. Stratiform precipitation in regions of convection: A meteorological paradox? *Bulletin of the American Meteorological Society,* **1997**, *78* (10): 2179–2196.
[39] Stevens B, Feingold G. Untangling aerosol effects on clouds and precipitation in a buffered system. *Nature,* **2009**, *461* (7264): 607–613.

DOI: 10.52396/JUSTC-2021-0238
JUSTC, **2022**, 52(2): 3